Consequences of magnetic ordering in chiral $Mn_{1/3}NbS_2$

Sunil K. Karna,[1,*] F. N. Womack,[1] R. Chapai,[1] D. P. Young,[1] M. Marshall,[2] Weiwei Xie,[2] D. Graf,[3] Yan Wu,[4] Huibo Cao,[4] L. DeBeer-Schmitt,[4] P. W. Adams,[1] R. Jin,[1] and J. F. DiTusa[1,*]

[1]*Department of Physics and Astronomy, Louisiana State University, Baton Rouge, Louisiana 70803, USA*
[2]*Department of Chemistry, Louisiana State University, Baton Rouge, Louisiana 70803, USA*
[3]*National High Magnetic Field Laboratory, Florida State University, Tallahassee, Florida 32310, USA*
[4]*Neutron Scattering Division, Oak Ridge National Laboratory, Oak Ridge, Tennessee 37831, USA*

(Received 29 April 2019; revised manuscript received 9 October 2019; published 11 November 2019)

We have investigated the structural, magnetic, thermodynamic, and charge-transport properties of $Mn_{1/3}NbS_2$ single crystals through x-ray and neutron diffraction, magnetization, specific heat, magnetoresistance, and Hall-effect measurements. $Mn_{1/3}NbS_2$ displays a magnetic transition at $T_C \sim 45$ K with highly anisotropic behavior expected for a hexagonal-structured material. Below T_C, neutron diffraction reveals increased scattering near the structural Bragg peaks having a wider Q dependence along the c axis than the nuclear Bragg peaks. This indicates either a short-range ferromagnetic (FM) order with a domain size of ~250 nm along the c axis or a possible magnetic modulation with a large pitch length. The expectation of a significant Dzyaloshinskii-Moriya interaction in this chiral-structured magnet, along with the helical state discovered in isostructural $Cr_{1/3}NbS_2$, suggest either a long period helical state with $q \sim 0.0025$ Å^{-1}, or FM regions separated by magnetic solitons, may be responsible for the apparent small size of the FM domains. Here, the domain length along the c axis is substantially larger than the pitch length of 48 nm found for the helimagnetic state in $Cr_{1/3}NbS_2$. Specific-heat-capacity measurements confirm a second-order magnetic phase transition with a substantial magnetic contribution that persists to low temperature. The low-temperature specific-heat capacity is consistent with a large density of low-lying magnetic excitations that are likely associated with topologically interesting magnetic modes. Changes to the magnetoresistance, the magnetization, and the magnetic neutron diffraction, which become more apparent below 20 K, imply a modification in the character of the magnetic ordering corresponding to the magnetic contribution to the specific-heat capacity. These observations signify a more complex magnetic structure both at zero and finite fields for $Mn_{1/3}NbS_2$ than for the well-investigated $Cr_{1/3}NbS_2$.

DOI: 10.1103/PhysRevB.100.184413

I. INTRODUCTION

Chiral-structured magnetic materials have generated considerable attention due to the topological nature of their magnetic structures including the formation of noncollinear and noncoplanar spin textures with long length-scale modulations [1–5]. These magnets have promising ingredients for future nanometer-scale quantum-information technology applications. Here, the chirality of the magnetism is generated by the crystal symmetry and the related spin-orbit coupling that create an antisymmetric exchange interaction known as the Dzyaloshinskii-Moriya (DM) interaction. The DM interaction is typically one or two orders of magnitude weaker than the isotropic exchange coupling [6,7], and the competition between the DM interaction strength, D, and the exchange interaction, J, causes the appearance of spin textures with a left- or right-handed chirality, depending on the sign of D and the handedness of the crystal structure [8]. When an external magnetic field is applied above a small threshold value, the helimagnetic ordering can be modulated into particlelike spin textures, such as a skyrmion or magnetic soliton lattice [2,9].

The most well-known case of topological magnetism occurs in the cubic-structured, $B20$, silicides and germanides [2–4], where a skyrmion lattice state can be accessed for small fields and temperatures near the Curie temperature, T_C. More recently, topology was discovered to be key to the magnetic structures found in hexagonal and chiral-structured $Cr_{1/3}NbS_2$, whose strong anisotropy instead favors a novel magnetic chiral soliton lattice phase when exposed to small fields [9,10]. This unusual magnetic structure consists of a superlattice based on a periodic helical spin texture [9,11,12]. $Cr_{1/3}NbS_2$ is synthesized by intercalating Cr between the layers of planar $2H$-type NbS_2, creating a crystal structure with the noncentrosymmetric and chiral space group $P6_322$ [13–15]. Its unique magnetic properties arise from the strong uniaxial anisotropy (easy plane) along with $S = 3/2$ Cr^{3+} magnetic moments. In addition, there is a small density of electronic charge carriers creating a highly anisotropic metal. As a result, $Cr_{1/3}NbS_2$ displays a helical magnetic ground state below 127 K with a small wave vector, $q \sim 0.015$ Å^{-1}, along the c axis [16,17]. The application of small magnetic fields can lead to a simple conical magnetic phase for $H//c$, or a novel chiral soliton lattice for $H//ab$ [9].

The ability to intercalate a wide variety of elements between the van der Waals bonded layers of NbS_2 allows us

*Corresponding authors: karna1@lsu.edu; ditusa@phys.lsu.edu

to question if unique magnetic structures and behaviors can be accessed by intercalating other transition-metal (TM) species, or if the same magnetic states are accessed as in $Cr_{1/3}NbS_2$. The wide variations to the helical and skyrmion lattice states found in the binary magnetic *B*20's lead us to posit that there will be fundamental modifications to the magnetic structures found in $TM_{1/3}NbS_2$ with changes in the intercalated species. Here, we report the synthesis of Mn-intercalated NbS_2, $Mn_{1/3}NbS_2$, in single-crystal form and the investigation of its magnetic, thermodynamic, and charge-transport properties [14,18–22]. A magnetic phase diagram was recently suggested based upon magnetization (M) measurements [20]. The data presented here largely reinforce our supposition that Mn intercalation results in fundamental changes to the magnetic structure and dynamics and is consistent with the results of this previous investigation [20] outside of details of the critical regime. We find a highly anisotropic magnetization and a magnetic transition at $T_C = 45\,\mathrm{K}$ evident in the magnetic susceptibility, specific heat, and resistivity. Neutron diffraction indicates a short-range ferromagnetic (FM) ordering along the c axis. Because there is no indication of crystalline disorder in either single-crystal x-ray diffraction, or neutron diffraction, on the same length scale, we consider other causes for the apparent small domain size for the FM ordering. The most obvious of these is the DM interaction, which tends to cause modulations of the magnetization direction. The implication is that $Mn_{1/3}NbS_2$ may host either a long pitch length helical state or, perhaps, ferromagnetic domains separated by magnetic solitons. Changes to the magnetization, charge transport, and specific-heat capacity with cooling below T_C and with the application of magnetic fields reveal behavior that is more complex than was observed in isostructural $Cr_{1/3}NbS_2$, suggesting a significant difference in the magnetic states both at zero and finite field.

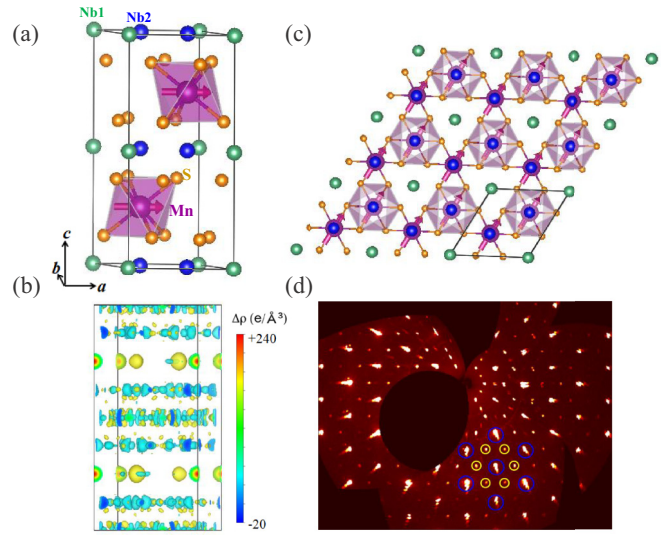

FIG. 1. Crystal and magnetic structure of $Mn_{1/3}NbS_2$. (a) Crystal structure demonstrating the intercalated Mn atoms which occupy the octahedral interstitial holes ($2c$ site) between trigonal prismatic layers of $2H$-NbS_2 in the ideal case. Arrows represent the Mn magnetic moments, as determined by a refinement of the neutron-scattering data. (b) Fourier map of electron-density residual structure factor $[(F_{obs}) - (F_{cal})]$ with a resolution of $0.05\,e^-/\text{Å}^3$. (c) Two-dimensional view of the crystal structure along the c axis highlighting the triangular network of Mn. The top Mn layer is indicated via shading of the surrounding octahedron of sulfur. (d) Diffraction precession image of the (HK0) plane of the reciprocal lattice. All of the resolved intensity peaks have been identified with the crystal lattice structure of the chiral space group $P6_322$. Blue circles identify reflections expected for the CdI_2 structure type of the underlying NbS_2 lattice, while reflections identified with yellow circles confirm the symmetry expected for the $P6_322$ space group. The flaring associated with reflections such as those enclosed by blue circles is instrumental in origin.

II. EXPERIMENTAL DETAILS

Single crystals of $Mn_{1/3}NbS_2$ were grown by iodine vapor transport with a central furnace temperature of 950 °C and a tube end temperature of 800 °C, as described in Ref. [18]. Powder x-ray-diffraction (PXRD) measurements on crushed crystals were carried out on a PANalytical Empyrean multistage x-ray diffractometer with Cu Kα radiation ($\lambda = 1.540\,59$ Å). These confirmed the Nb_3MnS_6 hexagonal crystal structure (space group $P6_322$), as shown in Figs. 1(a) and 1(c) with no apparent impurity phases. Single-crystal x-ray diffraction was performed on crystals mounted on the tip of a Kapton loop. Room-temperature (296 K) data were collected on a Bruker Apex II x-ray diffractometer with Mo Kα_1 radiation ($\lambda = 0.710\,73$ Å). Data were collected over a full sphere of reciprocal space with 0.5° scans in ω and an exposure time of 10 s per frame using SMART software for data acquisition. The 2θ range extended from 4° to 75°. Intensities were extracted and corrected for Lorentz and polarization effects with the SAINT program. Numerical absorption corrections were accomplished with XPREP based on face-indexed absorption [23]. The crystal structures were solved using the SHELXTL package with direct methods and refined by full-matrix least squares on the square of the structure factor, F^2 [24]. Electron density Fourier maps were generated by WINGX [25]. The single-crystal x-ray diffraction confirmed the crystal structure determined from PXRD. After locating all the atomic positions, the displacement parameters were refined as anisotropic, and weighting schemes were applied during the final stages of the refinement. The refinement showed that there was some site disorder apparent for the intercalated Mn. The refinement was consistent with 85% of the Mn on the expected $2c$ site (1/3, 2/3, 1/4) [as displayed in Fig. 1(a)], while an anomalous high electron-density residual ($+6.18\,e^-/\text{Å}^3$) on the $2b$ site (0, 0, 1/4) indicated partial occupancy of the Mn atoms. The single-crystal refinement details are included in the Supplemental Material, Tables S1–S3 [26]. To confirm the atomic distributions in $Mn_{1/3}NbS_2$, a Fourier map of electron-density residuals is presented in Fig. 1(b), showing the difference between the observed (F_{obs}) and calculated (F_{cal}) structure factors. The electron-density residuals on both the $2c$ and $2b$ sites demonstrate that Mn atoms partially occupy both sites. To check that the ordered structure corresponds to a superlattice, we carefully examined the diffraction precession image of the (HK0) plane shown in Fig. 1(d). The reflections marked with blue circles represent the trigonal CdI_2 type ($1T$ type) structure and the reflections

indicated by yellow circles provide proof of the ordered superlattice structure type $Mn_{1/3}NbS_2$ with the $P6_322$ space group.

Chemical analyses were performed using a JEOL JSX-8230 SuperProbe electron probe microanalyzer. This instrument allows simultaneous measurement via wavelength-dispersive spectroscopy (WDS) and energy-dispersive spectroscopy techniques. WDS determined a chemical composition of $Nb_{2.97}Mn_{1.03}S_{6.03}$, hereafter referred to as $Mn_{1/3}NbS_2$. We carefully checked for any indication of iodine in the WDS measurements of these crystals, finding no signal above background.

The magnetic structure of our single crystals was investigated via neutron diffraction performed at the four-circle diffractometer HB3A at Oak Ridge National Laboratory (ORNL). Reflections were collected at $T = 5$, 55, and 100 K, using a wavelength of 1.550 Å from a perfect bent Si-220 monochromator [27] for the magnetic structure determination. Refinements of the magnetic structure were performed with the FULLPROF suite [28]. In addition, we performed L scans [in the usual notation (HKL) to identify the reciprocal lattice] in proximity to the (011) nuclear Bragg peak with a larger wavelength, $\lambda = 2.541$ Å (Si-111 monochromator), for a series of temperatures between 5 and 55 K. Rocking scans were performed to characterize the mosaic spread of the crystal. The full width at half maximum (FWHM) of the (002) and (011) reflections are 0.195(7) and 0.25(1)°, respectively, at 100 K, indicating a high crystal quality.

Magnetization and magnetic susceptibility measurements with a magnetic field applied parallel and perpendicular to the crystallographic c axis were carried out in a Quantum Design (QD) Magnetic Property Measurement System superconducting quantum interference device magnetometer. These included ac susceptibility measurements performed at a frequency of 100 Hz with an ac driving amplitude of 3.9 Oe. The electrical resistivity and magnetoresistance (MR) were measured on single crystals with contacts formed via conductive epoxy (Epotek H20E) and thin platinum wire. These measurements were standard four-terminal ac resistance measurements with a current of 3 mA at a frequency of 17 Hz applied parallel to the ab plane of our crystals. Data was collected in a QD Physical Property Measurement System (PPMS) in a 90-kOe superconducting magnet, and in a 350-kOe resistive magnet at the National High Magnetic Field Lab in Tallahassee, FL. The MR was corrected for possible misalignment of the contacts by symmetrizing the data for positive and negative fields. Similarly, the Hall effect was measured with current and voltage contacts defined on the top of a c-axis oriented crystal. These measurements were carried out using an ac current of 3 mA and were corrected for misalignment of the leads by symmetrizing the data for positive and negative fields oriented along the crystallographic c axis. The specific-heat capacity was measured using a time-relaxation method in a QD PPMS between 2 and 100 K with magnetic fields of up to 90 kOe applied parallel and perpendicular to the c axis.

III. RESULTS AND DISCUSSION

After establishing the crystal structure and the site occupancy for the intercalated Mn, the temperature dependence of the magnetic susceptibility, χ, for H parallel and perpendicular to the c axis was measured and is presented in Figs. 2(a), 2(c), and 2(d). The temperature, T, dependence of the magnetic susceptibility indicates a magnetic transition at $T_C \sim 45$ K, and a large anisotropy below T_C, both of which are consistent with earlier measurements [14]. A fit of the Curie-Weiss (CW) law to the data for $H = 90$ Oe parallel to the c axis at temperatures between 150 and 350 K yields a Weiss temperature of theta, $\Theta \approx 61.6$ K (theta, $\Theta \approx 59.7$ K for $H \perp c$ axis) as shown in the inset to Fig. 2(a), indicating ferromagnetic interactions of the magnetic moments. The difference in Θ and T_C, with $\Theta > T_C$, likely reflects the layered structure of this material resulting in quasi-two-dimensional magnetic interactions. The best fit resulted in a Curie constant of $C = 2.88$ emu K/mol corresponding to a fluctuating magnetic moment of 4.80 μ_B (4.97 μ_B for $H \perp c$ axis), which suggests Mn^{3+} with $S = 2$. The magnetic moment found from the CW fitting procedure is in good agreement with the $4.8 - 5.1$-μ_B value reported in previous literature [18,19], but is significantly larger than that predicted by electronic structure calculations (3.8 μ_B) [29]. A very small anomaly at ~105 K, which corresponds to the magnetic transition temperature of $Mn_{1/4}NbS_2$, is observed in $\chi(T)$ and was avoided in the temperature range over which the fits were performed [30,31]. The magnetic susceptibility was measured under both zero-field-cooled (ZFC) and field-cooled (FC) conditions at $H = 5$ Oe [Figs. 2(c) and 2(d)] with a significant history dependence apparent below ~45 K as reported in Ref. [20]. This is similar to what was observed in $Cr_{1/3}NbS_2$ [32].

The anisotropic nature of the low-temperature magnetism suggested by the layered crystal structure of $Mn_{1/3}NbS_2$ is also evident in the magnetization, $M(H)$, as demonstrated at a temperature of 2 K in Fig. 2(b). The anisotropy is similar to that observed in $Cr_{1/3}NbS_2$ [33]. The field dependence of magnetization, M, resembles that of ferromagnetic materials with a saturation field near 0.5 kOe for a magnetic field, H, perpendicular to the c axis, and about 40 kOe for H parallel to the c axis. We note that the saturation fields we observe are substantially different from an earlier measurement [14], but are largely consistent with more recently published data [20], and we are unsure of the reason for the discrepancy. The size of the saturated magnetic moment, ~4.1 μ_B, is smaller than the magnetic moment determined from the Curie constant and is closer to expectations for a Mn^{4+} ion, although it is somewhat larger than that expected from electronic structure calculations [29]. The discrepancy in the magnetic moments determined from $\chi(T)$ and the saturated magnetic moment suggests that the magnetism may have some itinerant character and we point out that a similar discrepancy has been reported in $Cr_{1/3}NbS_2$ [13,19,33].

In light of the interesting magnetic structures found in $Cr_{1/3}NbS_2$, we have investigated the magnetic structure of $Mn_{1/3}NbS_2$ through single-crystal neutron diffraction. We collected 110 reflections at 5 K to characterize the magnetic ordering. In addition, we selected a weak nuclear Bragg peak (0 1 1) to track the magnetic order by scanning through (0 1 1) along the reciprocal L direction in consideration of the overlap of the magnetic scattering and the nuclear reflections. Representative data are shown in Fig. 3(a), where a scan along the L direction is displayed at 5 and 50 K. The scattering

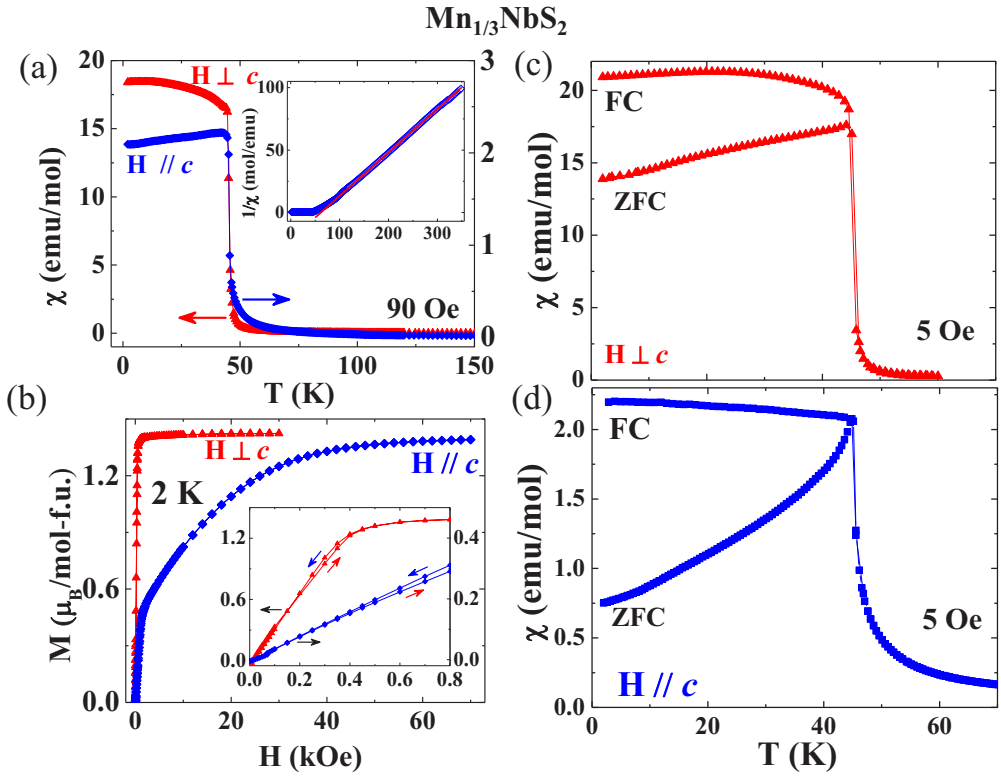

FIG. 2. Magnetic susceptibility and magnetization of $Mn_{1/3}NbS_2$. (a) Temperature, T, dependence and anisotropy of the magnetic susceptibility, χ, taken with a field $H = 90$ Oe. Inset: $1/\chi$ vs T for H parallel to the c axis. Line is a fit of the Curie-Weiss form to the data for $150 < T < 350$ K. (b) Magnetization, M, vs magnetic field, H, at 2 K with H parallel and perpendicular to the c axis. Inset: low-field M. T dependence of the FC and ZFC magnetic susceptibility at $H = 5$ Oe with (c) $H \perp c$ and (d) $H//c$.

associated with the magnetic ordering is clearly observed at 5 K as the intensity has increased dramatically from that at 50 K. The increased scattering in proximity to a nuclear Bragg peak indicates that the magnetism is nearly ferromagnetic. However, a closer inspection of the data in Fig. 3(a) including fitting the data to a simple Gaussian reveals changes that are not consistent with a simple ferromagnetic ordering. The results of this straightforward analysis are presented in Fig. 3(b) where the FWHM along L and the integrated intensity, I, from the peak centered at (0 1 1) is displayed for temperatures between 5 and 55 K. Here, $I(T)$ is consistent with a magnetic ordering at $T_C \sim 45$ K while the FWHM displays nonmonotonic temperature dependence below T_C. The FWHM increases by as much as 50%, indicating a more disordered or complex magnetic ordering. Furthermore, we have also performed a magnetic- and nuclear-structure refinement based on the reflections collected at 5 K. Here we assume a ferromagnetic structure by ignoring the broadened magnetic scattering and include the fact that 85% of the Mn resides on the *2c* site. The refinement indicates that the magnetic moments are confined to the crystallographic *ab* plane, similar to the case of $Cr_{1/3}NbS_2$ [10], and that the magnetic moment has a magnitude of 4.3(2) μ_B, slightly higher than the magnetic moment obtained from NMR measurements [21]. In order to compare more directly with $Cr_{1/3}NbS_2$, we have also performed a refinement to a long pitch length helical state with q held constant at $(0\,0\,q_c)$ with $q_c = 0.0025$ Å^{-1}. This procedure resulted in a similar value for the magnetic moment that was also confined to the *ab* plane. This magnetic moment is consistent with that found from the saturated magnetization.

The increased FWHM of the scattering evident below 50 K in Figs. 3(a) and 3(b) signifies a magnetic ordering that is inconsistent with long-range ferromagnetic order, which would result in magnetic scattering having the same FWHM as the nuclear Bragg peak. A FM ordering with a correlation length significantly smaller than that of the crystal structure is unusual as the nuclear Bragg peaks are indicative of small crystalline disorder. In addition, geometric frustration, low dimensionality, or chemical substitutions do not play a significant role in determining the magnetic structure of $Mn_{1/3}NbS_2$. This leads us to consider other possible causes for the increased FWHM of the magnetic scattering evident in Fig. 3. The most obvious cause for a short-ranged FM state in $Mn_{1/3}NbS_2$ is the DM interaction, which leads us to speculate that a modulated magnetic state, such as a helical or spin-density wave ground state, or perhaps FM regions separated by chiral magnetic solitons, may be present. The broadened FWHM in this case yields the scale of the pitch length or the size of the FM domains since the instrumental resolution is not sufficient to resolve the magnetic signal in close proximity to the nuclear Bragg peak. Because a significant DM interaction is anticipated [29] and a helical state has been well established in isostructural $Cr_{1/3}NbS_2$ [9,10], it is more likely that the magnetic state in $Mn_{1/3}NbS_2$ is an incommensurate one with a long pitch length. In addition, the conclusion from the refinement of the neutron-diffraction data

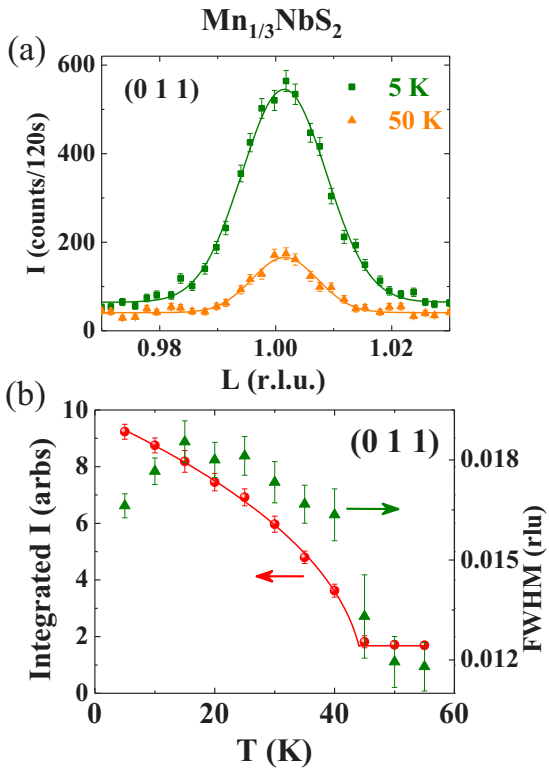

FIG. 3. Magnetic structure of $Mn_{1/3}NbS_2$. (a) Neutron-diffraction intensity, I, for a scan along the (0 1 L) direction in proximity to the (0 1 1) nuclear Bragg position. (b) T dependence of integrated intensity and full width at half maximum of the (0 1 1) reflection indicating magnetic ordering with a critical temperature T_C of 45 K. The solid line is a fit of a standard critical behavior model to the integrated intensity (see text).

that the magnetic moment lies in the *ab* plane (perpendicular to $\boldsymbol{q}$) suggests a helical state consistent with that found in other chiral-structured magnets. By fitting the magnetic contribution to the scattering in Fig. 3(a) to two Gaussians with a FWHM kept constant at the value determined by the width of the scattering peak at 50 K, we have made a rough estimate of $q \sim 0.0025$ Å^{-1} corresponding to a helimagnetic pitch length of $\lambda \sim 250$ nm, assuming a helical ground state. We note that this q is substantially smaller than that found in $Cr_{1/3}NbS_2$ (0.015 Å^{-1}) [10] and that our data are consistent with the q (pitch length of $\lambda \sim 300$ nm) reported in Ref. [22] for polycrystalline $Mn_{1/3}NbS_2$ samples. In addition, the long modulation length for FM ordering observed in $Mn_{1/3}NbS_2$ is compatible with expectations based upon electronic structure calculations [29]. We also note that there is a decrease in the FWHM of the (0 1 1) peak below 15 K, suggesting a possible change in the magnetic order at low temperatures.

The temperature dependence of the magnetic order parameter [Fig. 3(b)] can indicate the character of the magnetic ordering. Following a standard analysis, we fit the form $I = I_N + I_M(1 - T/T_C)^{2\beta}$ [34], where I_N represents the temperature-independent contribution from the nuclear reflection, and I_M indicates the magnetic intensity at saturation, to the integrated intensity data of Fig. 3(b) for $T < T_C$. The solid line in Fig. 3(b) represents the best fit of this form to the data with a value for the critical exponent $\beta = 0.23(3)$. This value of β lies between that expected for the three-dimensional Heisenberg model ($\beta = 0.38$) and the two-dimensional Ising model ($\beta = 0.125$), and close to that expected from a two-dimensional XY model. This is a reasonable result for a layered material such as $Mn_{1/3}NbS_2$. However, it is inconsistent with the value of $\beta = 0.37$ found in Ref. [20] from an Arrott analysis. We have attempted to fit the data of Fig. 3(b) with the standard dependence (above) while holding $\beta = 0.37$ constant and allowing the other parameters to vary without a finding a fit consistent with the error in our measurements.

After characterizing the magnetic properties of our $Mn_{1/3}NbS_2$ crystals, we explored their charge-transport properties to characterize the coupling between the magnetic and charge degrees of freedom. Figure 4(a) shows the temperature dependence of the in-plane electrical resistivity, ρ_{ab}, at magnetic fields, H, between 0 and 90 kOe. Note that ρ_{ab} exhibits metallic behavior with a residual resistivity ratio of ~64 signaling high-quality crystals with a long mean-free path of charge carriers. The behavior near the magnetic phase transition is similar to that of itinerant magnets with a sharp drop below T_C suggesting a significant reduction in the magnetic fluctuation scattering with magnetic ordering. The application of field effectively smooths the anomaly around the critical temperature. The resistivity is reduced by as much as 40% for a 90-kOe and 70% for a 350-kOe [inset of Fig. 4(d)] field near T_C, which is a large negative magnetoresistance even when considering the expected reduction of scattering from magnetic fluctuations. The MR for in-plane currents is presented in Figs. 4(b), 4(c), and 4(d) for temperatures between 5 and 60 K for H oriented parallel to the c axis, as well as perpendicular to the c axis and parallel to the current (longitudinal MR). The MR for these two orientations of H are similar, as both are strongly negative at high fields. However, the MR for $H//c$ includes a positive contribution that is maximum at 10 K near 27 kOe [Figs. 4(b) and 4(c)], suggesting that it may be due to scattering from magnetic moments that are canted along the c axis with field. For comparison, we note that in isostructural $Cr_{1/3}NbS_2$, a positive MR has not been reported [35] for $H//c$, and the negative MR seen there for $H \perp c$ is approximately seven times smaller than we observe in $Mn_{1/3}NbS_2$ at 5 K and 70 kOe. The field dependence seen in Fig. 4 does not saturate despite $M(H)$ saturating near 0.5 kOe [Fig. 2(b)], suggesting a mechanism more complex than a simple field reduction in spin-disorder scattering. We note that the MR for $H \perp c$ resembles a small power-law form, which is confirmed by fits of the data (Fig. 4(d)) that indicate a reduction of the power law from 3/4 to 2/3 with increasing temperature from 5 to 40 K. A similar negative MR was observed in $Cr_{1/3}NbS_2$ for samples that are thinner than the helical pitch ($\leqslant 47$ nm) [36]. However, we observe no hysteresis or acute jumps in the MR of our bulk single crystal of $Mn_{1/3}NbS_2$.

To explore the origins of the positive MR for $H//c$, we have measured the ac susceptibility with the drive field in the same orientation over similar field and temperature ranges. Figure 5(a) displays the field dependence of the real part, χ', and Fig. 5(b) the imaginary part, χ'', of the ac magnetic susceptibility at the indicated temperatures. Here, a temperature-dependent contribution to $\chi'(H)$ is observed

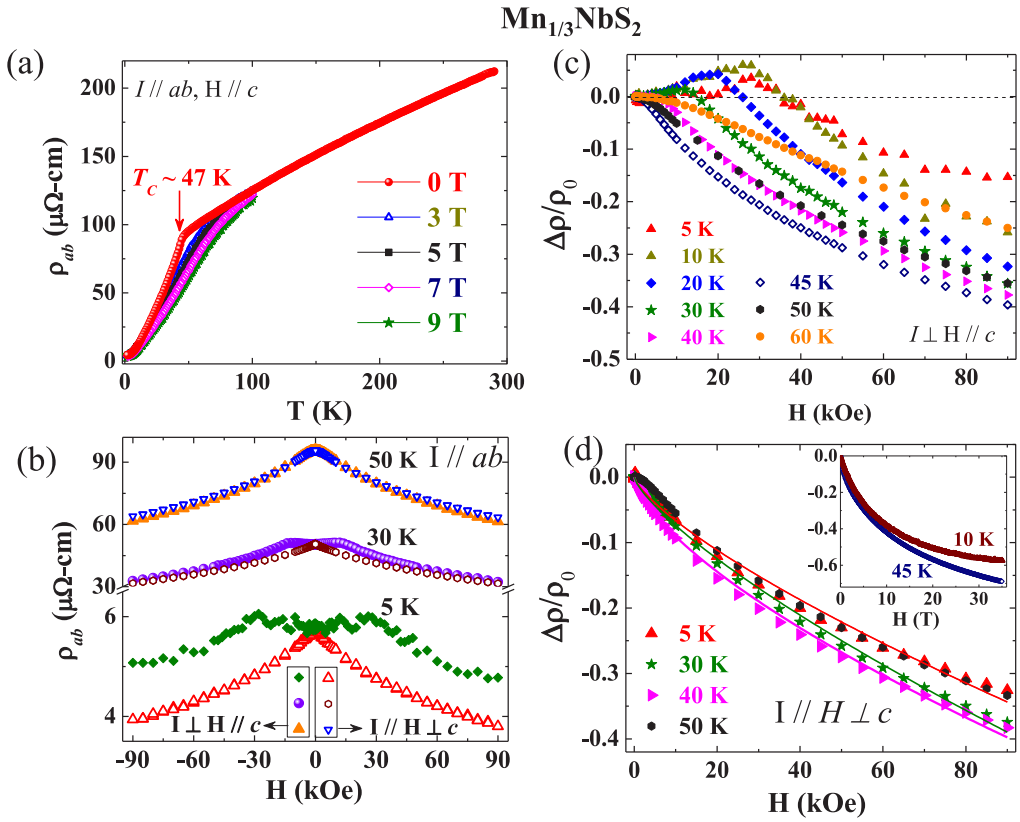

FIG. 4. Charge-transport properties of $Mn_{1/3}NbS_2$. (a) Temperature dependence of the resistivity measured with current, I, in the ab plane, ρ_{ab} at magnetic fields applied parallel to the c axis. (b) Magnetoresistance, $\rho_{ab}(H)$, with fields applied parallel (filled symbols) and perpendicular (open symbols) to I. Magnetoresistance, $\Delta\rho/\rho_0 = [\rho_{ab}(H) - -\rho_{ab}(0)]/\rho_{ab}(0)$, (MR) measured with H applied (c) parallel and (d) perpendicular to the c axis. The solid lines are fits of the form $\Delta\rho/\rho \sim H^{\alpha}$ to the data. Inset: MR at 10 and 45 K for H up to 350 kOe.

between 10 and 40 kOe for $T < T_C$ that is also apparent in the field derivative of the dc $M(H)$ in Fig. 5(d). To isolate this contribution, we present $\chi'(H)$ with the value at 45 K subtracted, $\chi' - \chi'_{45\,\mathrm{K}}$ in Fig. 5(c). Presenting the data in this manner makes it clear that the additional contribution to χ' is similar to the positive contribution to the MR, increasing in magnitude and having an increased characteristic field with cooling. We have quantified this behavior in the inset to Fig. 5(c), which compares the field of the zero crossing in the MR $[(\rho - \rho_0)/\rho_0 = 0]$ to the zero crossing of $\chi' - \chi'_{45\,\mathrm{K}}$. This comparison suggests a magnetic scattering origin for the positive component of the MR ($H//c$) and is comparable to a H-T phase diagram with both characteristic fields approaching zero at T_C.

To further characterize the charge transport, we present the Hall resistivity ρ_{xy} in Fig. 6 for temperatures between 5 and 70 K for current applied in the ab plane and magnetic fields oriented along the crystalline c axis. Data for three representative temperatures are shown in Fig. 6(a). Above T_C (at 70 K in the figure), ρ_{xy} is linear in H, consistent with holelike carriers. We note that the Hall voltage we measure is substantially smaller than that in $Co_{1/3}NbS_2$ [37] and $Cr_{1/3}NbS_2$ [33], suggesting a higher carrier density. As temperature T decreases below 50 K, an anomalous Hall effect (AHE) becomes apparent in ρ_{xy} with a strong negative contribution at low fields. The magnitude of the AHE is maximum in proximity to T_C, decreasing at lower temperatures as expected since ρ_{ab} decreases substantially below the magnetic ordering temperature [Fig. 4(a)]. The standard analysis of the Hall effect in magnetic materials considers two contributions, with $\rho_{xy} = R_0 H + 4\pi\ \mathrm{MR}_S$, where R_0 and R_S are the ordinary and anomalous Hall coefficients, respectively. In Fig. 6(b) ρ_{xy}/H as a function of M/H is displayed for temperatures spanning T_C, demonstrating the linear dependence expected from this standard form and allowing an accurate determination of both R_0 and R_S. The values of R_0 and R_S determined from linear fits to these data are shown in Fig. 6(c), with R_0 displaying a decrease of more than a factor of 2 below T_C, suggesting a significant change to the electronic structure with magnetic ordering. Within a simple single-band model, the estimated carrier concentration ($n = 1/|eR_0|$, where e is the electronic charge) is 2.7×10^{21} cm^{-3} at 70 K. In addition, R_S approaches zero at 5 K consistent with the small low-temperature ρ_{ab}, while the magnitude of R_S near T_C is large, being ~10 times larger than that in MnSi near its T_C of 29 K [38,39]. We observe no contributions to ρ_{xy}/H above background that are nonlinear in M/H, which would indicate a topological Hall effect or the unusual behavior observed in $Cr_{1/3}NbS_2$ [35]. Figure 6(d) presents the variation of the anomalous Hall parameter $S_H = R_S/{\rho_{ab}}^2$ as a function of T/T_C with no apparent T dependence, suggesting that the anomalous Hall effect is intrinsic in character.

The specific-heat capacity divided by temperature, $C_P(T)/T$, of $Mn_{1/3}NbS_2$ as a function of temperature is

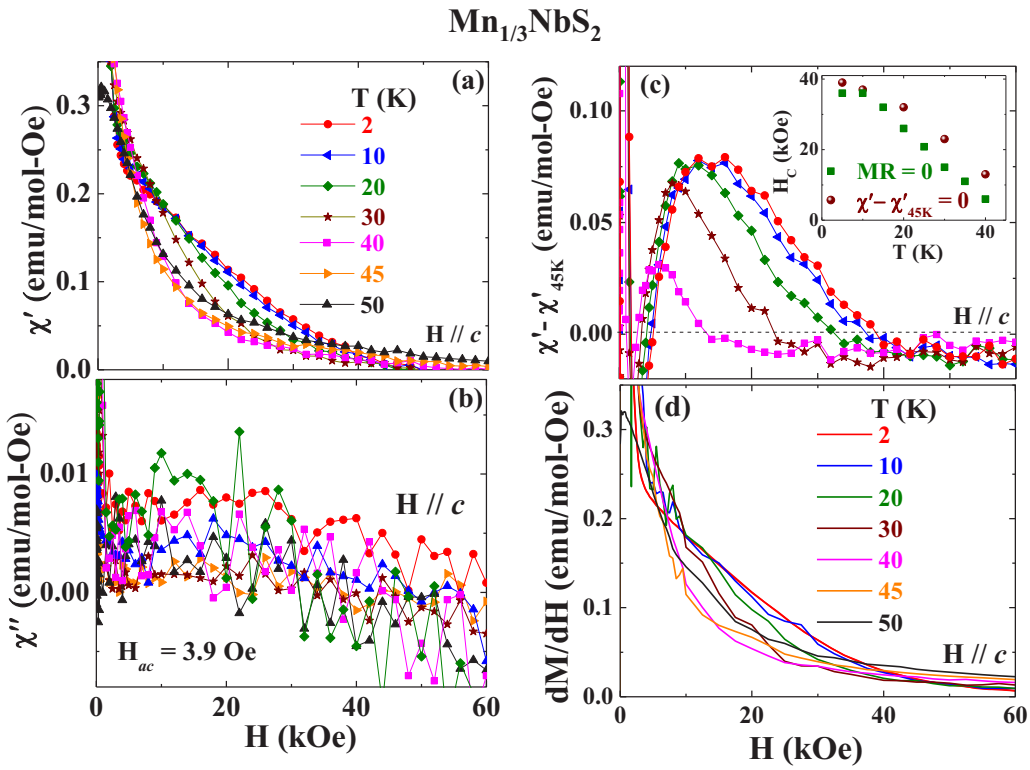

FIG. 5. Magnetic-field dependence of the ac magnetic susceptibility. (a) Real, χ', and (b) imaginary χ'' parts of the ac magnetic susceptibility vs magnetic field applied parallel to the c axis. (c) χ' after subtraction of χ' at 45 K, $\chi' - \chi'_{45\,\mathrm{K}}$. Inset: Zero-crossing fields for the MR [see Fig. 4(c)] and $\chi' - \chi'_{45\,\mathrm{K}}$ with H parallel to the c axis vs T. (d) Derivative of the magnetization with respect to H, dM/dH vs H with H parallel to the c axis.

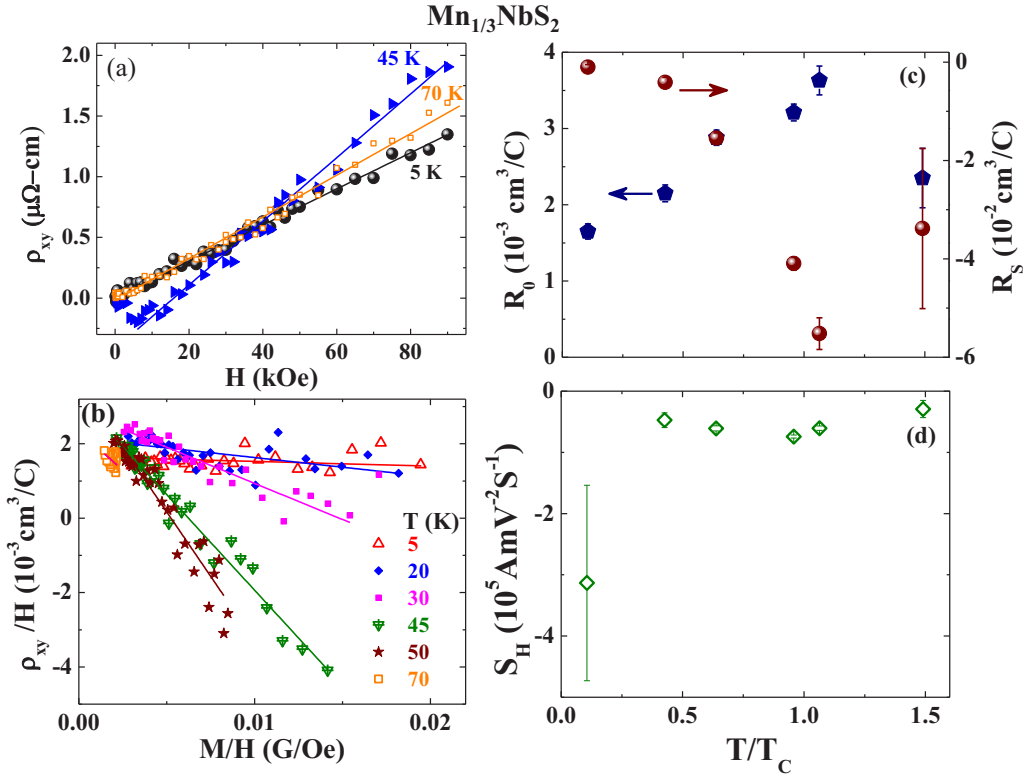

FIG. 6. Hall effect for $Mn_{1/3}NbS_2$. (a) Hall resistivity, ρ_{xy}, vs magnetic field, H, at 5, 45, and 70 K, (b) ρ_{xy}/H vs the magnetization divided by field (M/H), (c) Ordinary Hall coefficient R_0 and anomalous Hall coefficient, R_S, vs temperature divided by the Curie temperature (T/T_C), (d) Anomalous Hall parameter, $S_H (= R_S/\rho_{ab}{}^2)$ vs T/T_C.

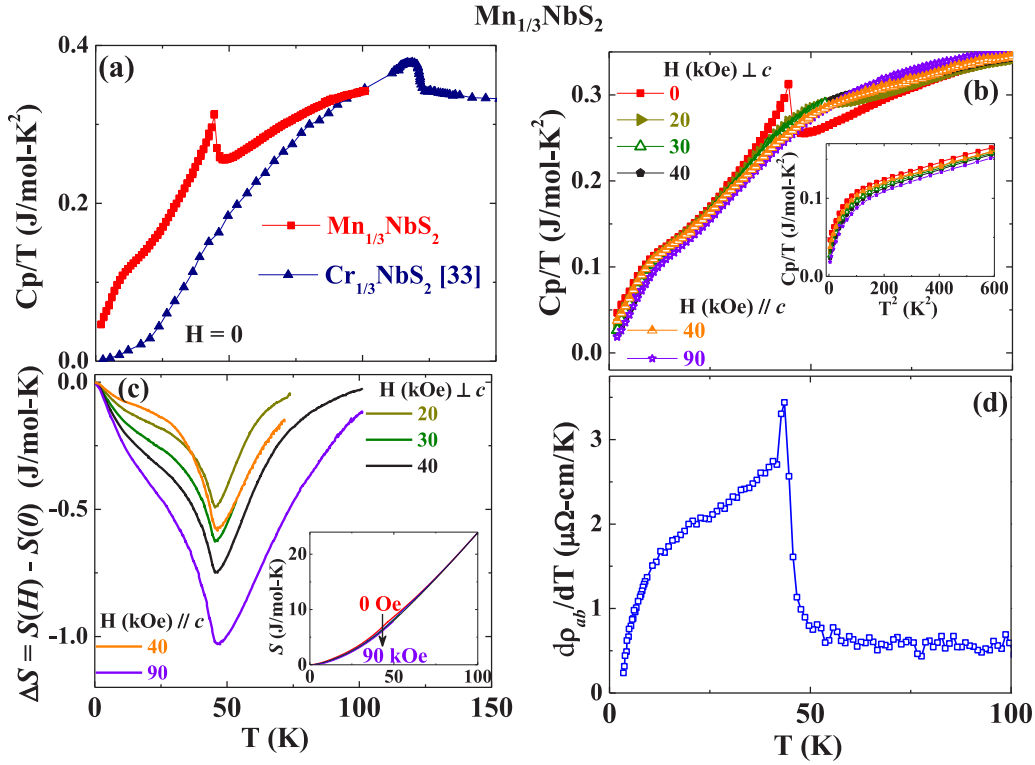

FIG. 7. Temperature and field dependence of the specific-heat capacity of $Mn_{1/3}NbS_2$. (a) Specific-heat capacity at constant pressure, C_P, divided by the temperature, T, vs T at zero magnetic field for $Mn_{1/3}NbS_2$. Data for $Cr_{1/3}NbS_2$ taken from Ref. [33] with permission of the authors. (b) T dependence of C_P for $0 \leqslant H \leqslant 9$ T. Inset: C_p/T vs T^2 at the same fields as in the main frame. (c) Change in entropy with application of field, $\Delta S = S(H) - -S(0)$, vs T. Inset: The entropy, S, determined from the integral of the data shown in frame (b). (d) The T derivative of the resistivity, $d\rho_{ab}/dT$ vs T.

displayed in Fig. 7(a) along with that of $Cr_{1/3}NbS_2$ from Ghimire *et al.* [33]. A sharp asymmetric peak is observed at the onset of magnetic ordering, indicating a second-order phase transition, similar in magnitude to that observed in $Cr_{1/3}NbS_2$. However, the magnitude of $C_P(T)/T$ of $Mn_{1/3}NbS_2$ remains much larger than that of $Cr_{1/3}NbS_2$ for all $T < T_C$, and the two display very different temperature dependencies. That the extra contribution to $C_P(T)/T$ in $Mn_{1/3}NbS_2$ originates from magnetic contributions is made clear by the large changes observed with the application of magnetic fields, shown in Fig. 7(b). In addition, whereas C_p/T of $Cr_{1/3}NbS_2$ at low temperature is well fit by a standard form for metals, $C_P/T = \gamma + \beta T^2$, with γ proportional to the density of states of the charge carriers and β related to Debye temperature, that of $Mn_{1/3}NbS_2$ cannot be well described by this form due to the significant magnetic contributions that survive to the lowest temperature measured (2 K). Including a term commonly used to model the C_p/T contribution due to magnons in ferromagnets, $\delta T^{1/2}$, did not result in reasonable values for the fit parameters. However, the similarity of C_p/T for $Mn_{1/3}NbS_2$ and $Cr_{1/3}NbS_2$ above T_C suggests a similar Debye temperature. The large low-temperature contribution to C_p/T for $Mn_{1/3}NbS_2$ implies that either $Mn_{1/3}NbS_2$ has a very small magnon stiffness, or there is a large density of other magnetic excitations available at low energies.

The effect of a magnetic field on the $C_P(T)/T$ is displayed over a wide temperature range in Fig. 7(b) for fields parallel or perpendicular to the c axis. Fields of a few tens of kOe are observed to effectively move entropy associated with the magnetic phase transition at T_C to temperatures of up to 80 K. This suggests large entropy changes with moderate magnetic fields. There are also significant differences in $C_P(T)/T$ with the orientation of the magnetic field particularly at low temperature with a stronger field dependence seen for fields perpendicular to the c axis.

To quantify the entropy, S, variation with field and temperature, $S(T,H)$, was found by numerically integrating $C_P(T)/T$ after extrapolation to $T = 0$, $S = \int_0^T \frac{C_p}{T} dT$. $S(T,H)$ calculated in this manner is displayed for a wide range of temperature and magnetic field shown in the inset to Fig. 7(c). The changes in entropy are further highlighted in the main frame of Fig. 7(c), where $\Delta S = S(H) - S(0)$ is presented and where significant changes are apparent across the entire temperature range probed for all fields. As expected, the largest $\Delta S(H)$ occurs near T_C. However, there are large decreases in entropy apparent over a wide temperature range, including for $T \ll T_C$ supporting the identification of the low-temperature contributions to $C_P(T)/T$ as originating from magnetic excitations. Furthermore, the anisotropy noted in the discussion of $C_P(T)/T$ is more obvious in Fig. 7(c) with the field orientation dependence of ΔS reflecting the smaller saturation fields for fields oriented perpendicular to the c axis. The similarity of the temperature derivative of the resistivity, $d\rho_{ab}/dT$, to $C_P(T)/T$, apparent in Fig. 7(d), makes clear that

the availability of a large density of low-energy magnetic excitations contributes significantly to the scattering of carriers. This observation strongly supports our assertion that the MR results from the suppression of magnetic scattering with field.

IV. DISCUSSION AND CONCLUSIONS

The previous section presented measurements that give an initial impression of the magnetic structure, the physical properties affected by the magnetic ordering, and the effect of magnetic excitations on the specific-heat capacity and charge transport both at $H = 0$ and for moderately sized magnetic fields for $Mn_{1/3}NbS_2$. The motivation was provided by the discovery of a magnetic soliton lattice in isostructural $Cr_{1/3}NbS_2$ in small fields aligned parallel to the NbS_2 planes [9]. The data presented here reveal many similarities between the two compounds along with indications of a longer length-scale modulation of the FM state (or possibly mesoscale FM domains separated by magnetic solitons) and a more complex behavior in the charge transport, ac susceptibility, and the magnetic contributions to the specific-heat capacity for $Mn_{1/3}NbS_2$. Perhaps the most significant of these is the specific-heat capacity, which reveals the presence of a much larger population of lower-lying excited states that are greatly affected by magnetic fields. These same excitations are likely to be the main scattering mechanism for charge carriers revealed by the MR, as well as the structure observed in the *ac* susceptibility between 10 and 40 kOe. The conclusion that follows directly from these observations is that the magnetic ordering and its response to magnetic fields is far richer in $Mn_{1/3}NbS_2$ than in $Cr_{1/3}NbS_2$, despite the crystalline structural similarity. This is important because the chiral crystal structure of these materials strongly suggests that magnetic excitations are topologically nontrivial and may offer the same advantages, including a robustness against decay to a topologically trivial magnetic state, that have attracted enormous attention to the skyrmion-lattice-hosting materials [1–5].

One possible source of low-lying states that may not offer topological excitations is the Mn site disorder that we have identified in our single-crystal x-ray-diffraction analysis. Here, we found that ∼15% of the intercalated Mn atoms reside on the crystallographic 2*b* site of the hexagonal lattice. The disorder introduced into the magnetic ordering and excitation spectra associated with this population of magnetic moments is not yet known. In addition, a comparison to the $Cr_{1/3}NbS_2$ samples used in previous measurements that found such interesting magnetic structures is not possible, as the level of site disorder for Cr is not reported. This is also true for published measurements on $Mn_{1/3}NbS_2$. However, our estimates of the entropy contribution expected for this population of magnetic moments based upon the measured magnetic moments that we have deduced from our magnetization measurements, and the density of defect sites indicated by our x-ray data is $S_{mag} = nR\ln(2J + 1) = 0.44\,\mathrm{J/mol\,K}$. This can account for less than 1/7 of the entropy difference between $Mn_{1/3}NbS_2$ and $Cr_{1/3}NbS_2$ apparent in the inset to Fig. 7(c) ($S_{mag} = 3.25\,\mathrm{J/mol\,K}$ below 37 K), even when accounting for the differences in magnetic ordering temperatures. Therefore, we conclude that the site disorder alone is not the cause for the large differences between the $Mn_{1/3}NbS_2$ and $Cr_{1/3}NbS_2$, at least in the simple case where the Mn atoms residing on the 2*b* sites act as relatively uncoupled magnetic moments. Thus, the enhanced specific-heat capacity at temperatures well below T_C must involve the Mn on the 2*c* site, which orders at 45 K, implying that the constraints on the magnetic structure due to the crystal-structure symmetry must also hold for these low-lying modes. A second possible source for low-lying magnetic excitations could follow from stacking disorder of the NbS_2 planes along the *c* axis, although more in-depth investigation of the crystal structure of our samples is needed to assess this possibility.

In summary, we have measured the structural, magnetic, magnetic structural, charge transport, and thermodynamic properties of $Mn_{1/3}NbS_2$ and compared them with published data on $Cr_{1/3}NbS_2$. We find largely similar behavior, including a nearly ferromagnetic ordering. Although our neutron-diffraction experiment lacked the resolution to resolve the magnetic structure, it is suggestive of either a short-ranged FM ordering (with a temperature-dependent correlation length) or a long length modulation, significantly longer than that found in $Cr_{1/3}NbS_2$. The resistivity and Hall effect are consistent with a strong coupling of magnetic and charge-transport properties. In addition, the specific-heat capacity indicates a large density of low-lying magnetic excitations that is absent in $Cr_{1/3}NbS_2$. The low-temperature specific-heat capacity is broadly consistent with a very low spin wave stiffness, but is more likely to be associated with topologically interesting magnetic modes. The appearance of a positive MR for $H//c$ that correlates well to features in the magnetic response and the magnetic contribution to the specific-heat capacity, as well as a decrease in the width of the magnetic scattering peaks for neutron diffraction, may be indicators of these topological excitations. Thus, further investigation of the magnetic structure and excitation spectrum of the material will likely yield fruitful discoveries in this prototypical chiral-structured magnet.

ACKNOWLEDGMENTS

This material is based upon the work supported by the U.S. Department of Energy under EPSCoR Grant No. DE-SC0012432 with additional support from the Louisiana Board of Regents. P.W.A. acknowledges the financial support for the specific heat measurements from the U.S. Department of Energy, Office of Science, Basic Energy Sciences, under Award No. DE-FG02-07ER46420. A portion of this work was performed at the National High Magnetic Field Laboratory, which is supported by the National Science Foundation Cooperative Agreement No. DMR-1644779 and the State of Florida. The work at ORNL's HFIR was sponsored by the Scientific User Facilities Division, Office of Science, Basic Energy Sciences (BES), U.S. Department of Energy (DOE). H.B.C. acknowledges support of the neutron measurements from a U.S. DOE BES Early Career Award No. KC0402010 under Contract No. DE-AC05-00OR22725.

[1] U. K. Rössler, A. N. Bogdanov, and C. Pfleiderer, Nature (London) **442**, 797 (2006).

[2] S. Mühlbauer, B. Binz, F. Jonietz, C. Pfleiderer, A. Rosch, A. Neubauer, R. Georgii, and P. Böni, Science **323**, 915 (2009).

[3] X. Z. Yu, Y. Onose, N. Kanazawa, J. Park, J. Han, Y. Matsui, N. Nagaosa, and Y. Tokura, Nature (London) **465**, 901 (2010).

[4] X. Z. Yu, N. Kanazawa, Y. Onose, K. Kimoto, W. Z. Zhang, S. Ishiwata, Y. Matsui, and Y. Tokura, Nat. Mater. **10**, 106 (2011).

[5] S. Seki, X. Z. Yu, S. Ishiwata, and Y. Tokura, Science **336**, 198 (2012).

[6] I. Dzyaloshinsky, J. Phys. Chem. Solids **4**, 241 (1958).

[7] T. Moriya, Phys. Rev. **120**, 91 (1960).

[8] A. Bauer and C. Pfleiderer, Phys. Rev. B **85**, 214418 (2012).

[9] Y. Togawa, T. Koyama, K. Takayanagi, S. Mori, Y. Kousaka, J. Akimitsu, S. Nishihara, K. Inoue, A. S. Ovchinnikov, and J. Kishine, Phys. Rev. Lett. **108**, 107202 (2012).

[10] T. Miyadai, K. Kikuchi, H. Kondo, S. Sakka, M. Arai, and Y. Isikawa, J. Phys. Soc. Jpn. **52**, 1394 (1983).

[11] Y. Togawa, Y. Kousaka, S. Nishihara, K. Inoue, J. Akimitsu, A. S. Ovchinnikov, and J. Kishine, Phys. Rev. Lett. **111**, 197204 (2013).

[12] Y. Masaki and R. L. Stamps, Phys. Rev. B **95**, 024418 (2017).

[13] S. S. P. Parkin and R. H. Friend, Philos. Mag. **41**, 65 (1980).

[14] Y. Kousaka, Y. Nakao, J. Kishine, M. Akita, K. Inoue, and J. Akimitsu, Nucl. Instrum. Methods Phys. Res. Sect. A **600**, 250 (2009).

[15] B. Van Laar, H. M. Rietveld, and D. J. W. Ijdo, J. Solid State Chem. **3**, 154 (1971).

[16] T. Moriya and T. Miyadai, Solid State Commun. **42**, 209 (1982).

[17] M. N. Wilson, A. B. Butenko, A. N. Bogdanov, and T. L. Monchesky, Phys. Rev. B **89**, 094411 (2014).

[18] K. Anzenhofer, J. M. Van Den Berg, P. Cossee, and J. N. Helle, J. Phys. Chem. Solids **31**, 1057 (1970).

[19] J. M. Van den Berg and P. Cossee, Inorg. Chim. Acta **2**, 143 (1968).

[20] Y. Dai, W. Liu, Y. Wang, J. Fan, L. Pi, L. Zhang, and Y. Zhang, J. Phys.: Condens. Matter **31**, 195803 (2019).

[21] V. V. Ogloblichev, Yu. V. Piskunov, I. Yu. Arapova, and F. B. Mushenok, Phys. Met. Metallogr. **119**, 1056 (2018).

[22] Y. Kousaka, MLF Experimental Report of J-PARC (see https://j-parc.jp/researcher/MatLife/common/lists/2013B/BL08_2013B0133.pdf).

[23] *SHELXTL*, version 6.10, Bruker AXS Inc., Madison, WI, 2000.

[24] G. M. Sheldrick, Acta Cryst. Sect. A **64**, 112 (2008).

[25] L. J. Farrugia, J. Appl. Cryst. **45**, 849 (2012).

[26] See Supplemental Material at http://link.aps.org/supplemental/10.1103/PhysRevB.100.184413 for details on the structural refinement.

[27] B. C. Chakoumakos, H. B. Cao, F. Ye, A. D. Stoica, M. Popovici, M. Sundaram, W. Zhou, J. S. Hicks, G. W. Lynn, and R. A. Riedel, J. Appl. Cryst. **44**, 655 (2011).

[28] J. Rodriguez-Carvajal, Physica B **192**, 55 (1993).

[29] S. Mankovsky, S. Polesya, H. Ebert, and W. Bensch, Phys. Rev. B **94**, 184430 (2016).

[30] Y. Onuki, K. Ina, T. Hirai, and T. Komatsubara, J. Phys. Soc. Jpn. **55**, 347 (1986).

[31] The small anomaly at 105 K in the magnetic susceptibility indicates a very small density of MnNbS in our crystals. However, no indication of this impurity phase was apparent in either the x-ray or neutron-diffraction measurements.

[32] Y. Kousaka, T Ogura, J. Zhang, P. Miao, S. Lee, S. Torii, T. Kamiyama, J. Campo, K. Inoue, and J. Akimitsu, J. Phys.: Conf. Ser. **746**, 012061 (2016).

[33] N. J. Ghimire, M. A. McGuire, D. S. Parker, B. Sipos, S. Tang, J.-Q. Yan, B. C. Sales, and D. Mandrus, Phys. Rev. B **87**, 104403 (2013).

[34] T. Chatterji, *Neutron Scattering from Magnetic Materials* (Elsevier, Amsterdam, 2006).

[35] A. C. Bornstein, B. J. Chapman, N. J. Ghimire, D. G. Mandrus, D. S. Parker, and M. Lee, Phys. Rev. B **91**, 184401 (2015).

[36] L. Wang, N. Chepiga, D.-K. Ki, L. Li, F. Li, W. Zhu, Y. Kato, O. S. Ovchinnikova, F. Mila, I. Martin, D. Mandrus, and A. F. Morpurgo, Phys. Rev. Lett. **118**, 257203 (2017).

[37] N. J. Ghimire, A. S. Botana, J. S. Jiang, J. Zhang, Y.-S. Chen, and J. F. Mitchell, Nat. Commun. **9**, 3280 (2018).

[38] M. Lee, Y. Onose, Y. Tokura, and N. P. Ong, Phys. Rev. B **75**, 172403 (2007).

[39] N. Manyala, Y. Sidis, J. F. DiTusa, G. Aeppli, D. P. Young, and Z. Fisk, Nat. Mater. **3**, 255 (2004).